Peer-reviewed version available at Review of Scientific Instruments 2019, 90; doi:10.1063/1.5112374

Development of a new temperature measurement system for the observation of adiabatic shear band[a)]

R. Pawelko,[1, b)] V. Pina,[1] and P. Hervé[1]

L.E.M.E, Université Paris Nanterre, 50 Rue de Sèvres, 92410 Ville d'Avray, France

(Dated: 22 May 2019)

This paper presents the development of a new system designed to measure the local temperature field in adiabatic shear band. Transient temperature field are simultaneously recorded by an array of 32 InSb infrared (IR) detectors and a streak camera working in visible-near infrared (VIS-NIR). Observations in IR offer a low temperature detection limit (350 °C) but they are highly sensitive to uncertainty in the emissivity. Observations in VIS-NIR allow for measurement only at high temperatures (>750 °C) but they are less affected by uncertainty on emissivity and present a higher temperature sensitivity. By performing simultaneous measurements, it is possible to obtain data on a large temperature range with an improved accuracy at high temperature. The different sources of errors caused by uncertainty in the emissivity, spatial and temporal resolution of the detectors has been analyzed and an estimation of the total measurement uncertainty of the system is given.

[a)]The following article has been submitted to Review of Scientific Instruments. After it is published, it will be found at Link.

[b)]Electronic mail: romainpawelko@gmail.com

Peer-reviewed version available at Review of Scientific Instruments 2019, 90; doi:10.1063/1.5112374

I. INTRODUCTION

Adiabatic shear banding is a failure mode which occur in materials subject to dynamic loading. The formation of adiabatic shear band (ASB) comes from coupled thermomechanical phenomenon which produce an instability in the material leading to a catastrophic failure[1]. The conditions for the apparition of an instability is that the thermal softening effects become dominant over the strain hardening of the material[2], when this condition is satisfied the plastic deformation will stop been homogeneous and start to localize in a narrow band. While the localization occurs, some of the plastic work is converted into heat causing a local rise of the temperature and an increase of the thermal softening thus favoring the deformation and starting a catastrophic cycle. Those bands act as precursors of cracks initiation and propagation, they are often characterized as adiabatic because the rate of heat generation is usually much more important than the heat flux conducted away from the deforming zone. The formation of ASB is favoured by high strain rate, low thermal conductivity, low heat capacity and intense strain localization inside the band can lead high temperature rise close to the melting point of the material.

Because of the importance of thermomecanical coupling effects in the formation of ASB, temperature measurements are essentials to fully understand the phenomenon. Subsequently, several teams worked on the development of experimental set-ups to measure the ASB temperature and radiometry has emerged as the most appropriate method[3–7]. However temperature measurements in ASB present some difficulties inherent the phenomenon itself (size of the ASB, short time scale) or to the radiometric measurement (errors due to uncertainty in the emissivity).

We designed a new system based on simultaneous measurements in two different spectral ranges with one at short wavelengths leading to temperature measurements almost independent of emissivity variations. A detailed analysis of the system will be presented through a practical application allowing for the characterisation of the different sources of error and the calculation of realistic error bars. Results show that our system is able to measure the maximum temperature with an uncertainty of 7.5 % in VIS-NIR and 15 % in IR, confirming the benefit of short wavelengths observations.

For our study, a complete experimental setup has been designed which can be separated in three sub-assembly : the loading device, the optics and the detectors. Because the per-

formances of the measurement system are related to the architecture of these sub-assembly, they will be presented in detail in section II. In section III, we will identify the different sources of error and their influences on the temperature measurement, this analysis will allow us to give a global uncertainty estimation. In section IV we will present the results of temperature measurements for different configurations and analyse the true performance of our system.

II. SYSTEM DESIGN

A. Loading device

To reach the high strain rate necessary for the formation of ASB, a punch loading experiment has been designed. The main reason is that punch loading allow to predict precisely where ASB will form and this is of main importance because we want to be sure that Ashear bands will form in the observed area (less than $22\,\mu m \times 960\,\mu m$ for IR measurements). An other advantage is that the observed area on the sample is plane, thereby minimizing the defocusing problems that can arise with cylindrical specimen.

A schematic of the system is shown on Fig.1. The dynamical loading is produce by the impact of an aluminum cylinder on a punch made of quenched 100C6 steel. The gas gun allows for an impactor speed up to $100\,m\,s^{-1}$. The impactor velocity is measured using emitter-receiver pairs mounted at the muzzle end of the barrel.

The material used for our experiments is titanium alloy Ti-6Al-4V which is widely used in aerospace and known to be highly susceptible to adiabatic shear failure[1,6,8]. In order to get an identical surface roughness, all the samples has been polished ($R_a \approx 0.1$).

B. Detectors

When a surface emits thermal radiation, this radiation contains informations about the surface's temperature. A radiometer is a device that produce a signal which is a function of the incident radiation. Once the thermal radiation emits by the surface is known, it is possible to evaluate the temperature by using physical laws such as Planck's law or Stefan-Boltzmann law. For our experiments we used the luminance which is the spectral distribution of a blackbody emissive power per unit area per unit solid angle as a function of temperature

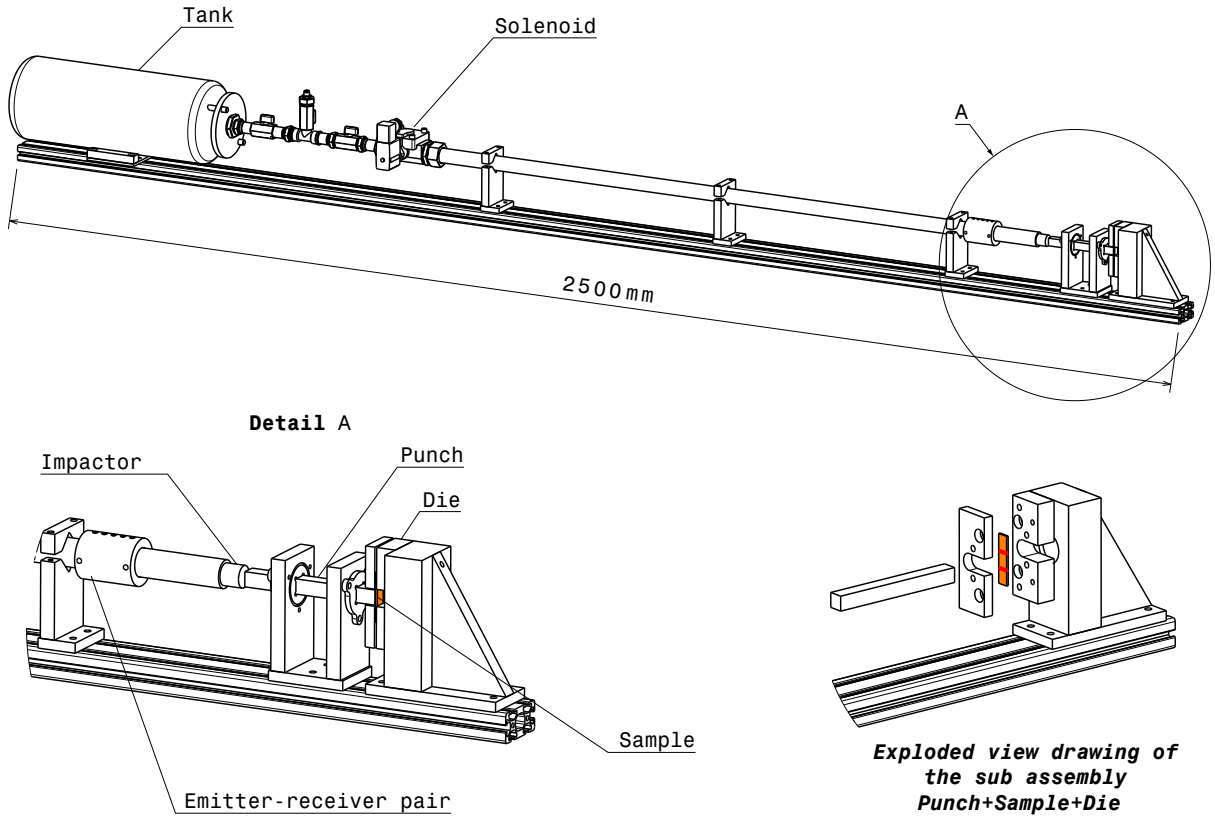

FIG. 1: Schematic of the punch loading equipment

T and wavelength λ :

$$L^0_\lambda(\lambda, T) = \frac{2\pi c_1}{\lambda^5 \exp\left(\frac{c_2}{\lambda T}\right) - 1} \tag{1}$$

with $c_1 = 5.9635 \times 10^7 \mathrm{W\,m^2\,\mu m^{-4}}$ and $c_2 = 14388 \mu\mathrm{m\,K}$. Expression 1 is define for a blackbody witch is a ideal emitter, for a real opaque surface the luminance is define as :

$$L_\lambda(\lambda, T) = \varepsilon(\lambda, T) \cdot L^0_\lambda(\lambda, T) \tag{2}$$

Where $\varepsilon(\lambda, T)$ is the spectral emissivity of the surface. The accuracy of the emissivity data is essential to perform precise temperature measurements; however, emissivity depends on various parameters such as material, temperature, wavelength, direction of observation, surface roughness and physical state of the material. For this reason, it is difficult to know precisely the value of the emissivity. We can estimate the influence of emissivity uncertainty on the temperature measurement, considering a monochromatic radiation, we can use an

approximation of the Planck's Law known as the Wien's law :

$$L^0_\lambda(\lambda, T) = \frac{2\pi c_1}{\lambda^5} \exp\left(\frac{-c_2}{\lambda T}\right) \tag{3}$$

If we calculate the differential form of equation 3 considering no error on luminance and wavelength ($\frac{dL^0_\lambda}{L^0_\lambda} = \frac{d\lambda}{\lambda} = 0$) we obtain the relation :

$$\frac{\Delta T}{T_V} = -\frac{\lambda T}{c_2} \cdot \frac{\Delta \varepsilon}{\varepsilon_V} \tag{4}$$

Where $\Delta\varepsilon = \varepsilon_L - \varepsilon_V$ is the difference between the supposed emissivity (ε_L) and true emissivity (ε_V). $\Delta T = T_L - T_V$ is the difference between luminance temperature (T_L) and true temperature of the surface (T_V). The luminance temperature correspond to the measured temperature if we consider ε_L instead of ε_V. Figure 2 show the error on measured temperature if we consider a theoretical emissivity $\varepsilon_L = 0.5$ while the true emissivity value lie between 0.01 and 0.99 ($\frac{\Delta\varepsilon}{\varepsilon_V} = \pm 0.98$). This example show the advantage of short wavelength measurement: even if we have almost no information on the true emissivity, we can see that for wavelengths below 1 µm, the maximum error is less than 10 % while it is above 50 % if we work at 5 µm.

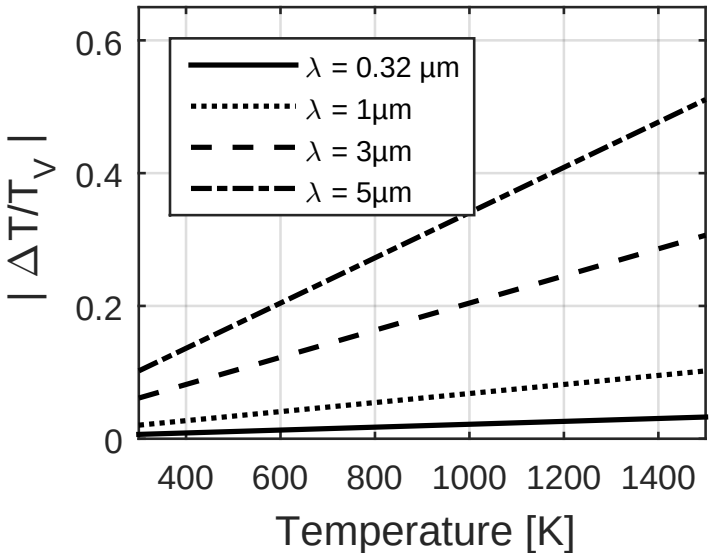

FIG. 2: Relative error on the temperature considering $\varepsilon_L = 0.5$ and $\frac{\Delta\varepsilon}{\varepsilon_V} = \pm 0.98$

The main drawback of short wavelength measurements is the lack of photons emitted at low temperatures. If we look at the evolution of luminance as a function of wavelength and

temperature, we see that there is a peak of emissive power shifting to the short wavelength as the temperature increase. The wavelength of maximum emissive power can be calculated using the Wien's displacement law :

$$\lambda_{max} = \frac{2897.8}{T} \approx \frac{c_2}{5T} \tag{5}$$

This relation show that at ambient temperature, the peak of emissive power will be close to 10 µm, so almost no photons will be emitted at short wavelengths, the temperature of the observed surface will need to increase to emit enough short wavelength photons, so that the detectors generates a signal above the noise level.

Because, short wavelength measurements are less sensitive to emissivity uncertainty but doesn't allow for low temperature observations, we designed our system to perform simultaneous measurements in IR and VIS-NIR taking advantage of each spectral range's specificity. Measurements in IR are made by an array of 32 InSb detectors with a dimension of 43×43 µm and a center line spacing of 61 µm. Those detectors are sensitive to radiation up to 5.56 µm and in order to limit thermal noise, they are cooled to 77K by liquid nitrogen. Each detector is associated with an amplification circuit, all channels are thus operating in parallel and can be monitor individually. While InSb detectors have a rise time of nanoseconds, amplifiers limit the practical frequency response to the MegaHertz range and lower, this is also mostly amplifiers that define the detectivity of the system. During our expermients, the signal from each detector is recorded independently at a sampling rate of 1 MHz using a multi-channel transient recorder (LDS Nicolet Genesis).

Measurements in VIS-NIR are made by an Optronis SC-10 streak camera which is constituted by three main subsystems: the streak tube, the image intensifier and the readout camera. The streak tube convert the incident photons into electrons, these electrons are then sweep onto a phosphor screen who convert the temporal evolution into a spatial variation. The streak tube is follow by an image intensifier that amplify the number of photons, the output image produce on the screen of the intensifier is then record by a readout camera. This system allow the detection of low light level with a high temporal resolution. Our camera is equipped with a 15 mm length input slit (spatial direction) with adjustable width (temporal direction), the S-25 photocathode has a spectral response range from 280 nm to 920 nm. The sweep unit allows large variety of sweep time from 5 ns to 100 ms, the temporal resolution of the camera depends on the sweep speed and the line spread function (see section

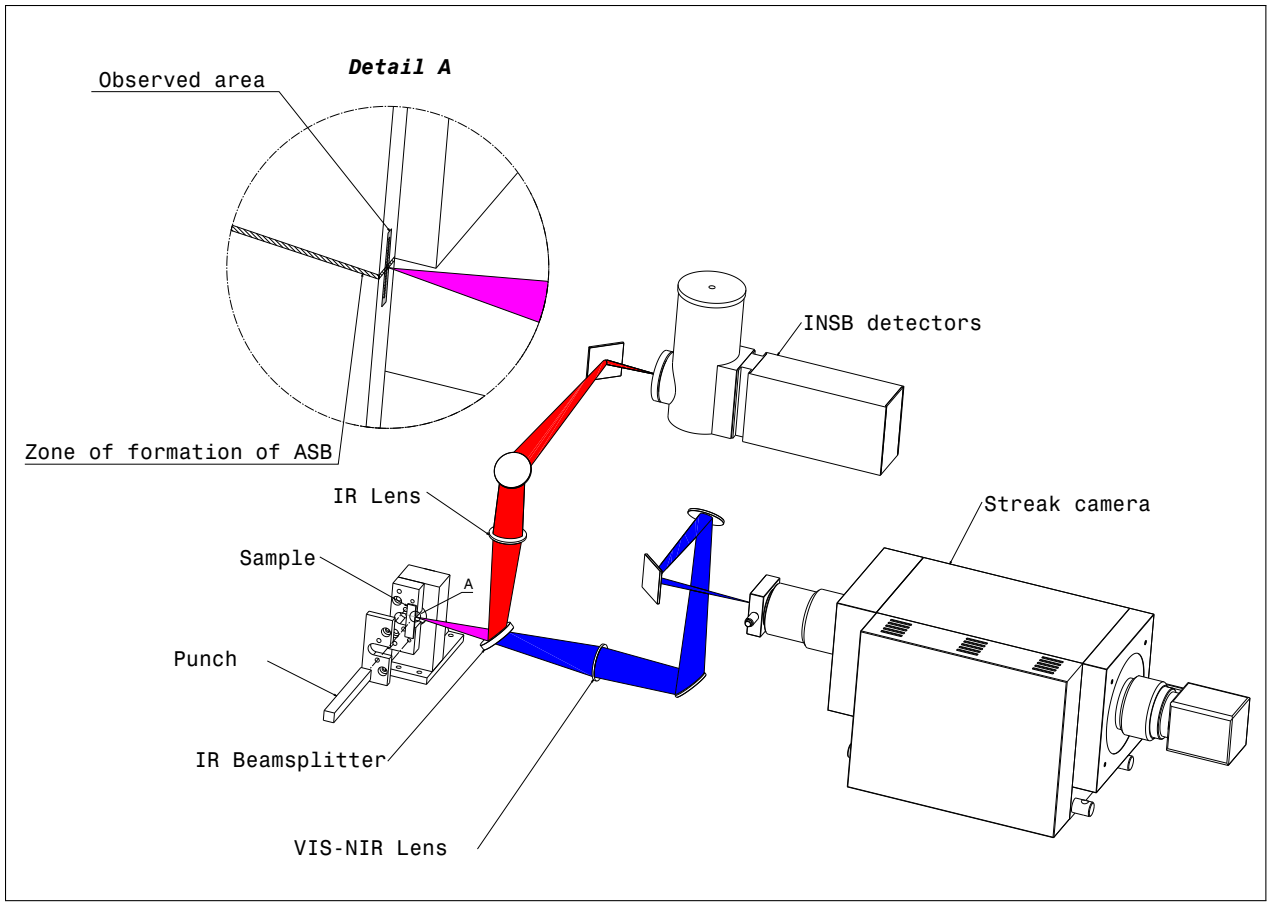

FIG. 3: Schematic of the optical assembly

III B). Streak cameras are specially design for the observation of high-speed phenomenons, they have been widely used in the field of detonation and shock-waves[9] and are well adapted to the study of ASB.

C. Optics

The role of the optical system is to focus the radiation emitted from the surface of the sample onto the detectors. Figure 3 presents a simplified scheme of the optical assembly, the red optical path correspond to IR and the blue correspond to VIS-NIR. The photon flux is divided by a 50:50 CaF_2 beamsplitter which offer a nearly constant beamsplitting ratio from 180 nm to 8 µm. In previous studies, most authors used mirrors or reflective objectives which are free of chromatic aberrations and can be use on a broad spectral range[3,4,6,10]. However these optical elements are really sensitive to alignment errors such as tilt or defocusing and

can easily present geometrical aberrations such as coma or distortion[10]. Reflective objectives also have the disadvantage of being poorly modular and are usually designed with short focal length which is not suitable with our assembly and the presence of the optical beamsplitter, for these reasons, our system has been designed with lenses. Because of the broad spectral range of our detectors, it is essential to use achromatic lenses which are combinations of two or three elements chosen such as the dispersion of one element is compensated by the others, these lenses are designed to correct the chromatic aberrations over a define spectral range by minimizing the focal shift. For the IR path, we selected an Si/Ge air-spaced achromatic doublet optimized for 3-5 µm range and for the streak camera we used a N-BAK4/N-SF10 doublet optimized for 0.4-1 µm range. The presence of the beamsplitter in our assembly imposes a minimal distance between collecting lenses and the sample (Fig. 3), this limitation forced us to use lenses with small numerical aperture: 1/20 for the IR and 1/2 for the VIS-NIR. Considering the size the detectors, we chose an optical magnification of 2 for the InSb array and 4 for the streak camera. To make temperature measurements on a line perpendicular to shear bands (see Detail A in Fig. 3) we used a set of two mirrors to flip the image by 90° on each path. The alignment of all the elements has been made using a laser beam, then the focusing of the detectors was performed before each experiment using a Globar and a dummy specimen with a 50 µm slit.

D. Calibration

The response of each detector-optics sub-assembly to a given heat signal as been determined experimentally. The calibration procedure consists of placing a black body at the location of the sample and record the output signals of the detector along with the black body corresponding temperatures, then Ti-6Al-4V calibration curves has been calculated considering emissivity data of the material[11,12] (see section III C 1 and III C 2). Both detector calibration curves are displayed on figure 4 along with their noise equivalent temperatures. For InSb, we noted the presence of cross-talk effects when all the channels are operating, similar phenomenon has been observed by Rittel[13]. The presence of cross-talk effects forced us to reduce as much as possible the bandwidth of each channel in order to minimize the noise, for this reason we chose a bandwidth of 13 kHz. In this configuration the minimum detectable temperature in IR is 550 K so InSb will be able to record most of

the third stage of ASB formation which correspond to the fully formed ASB[3].

For the streak camera, curves in Fig. 4 correspond to a sweep speed of $50\,\mu s\,mm^{-1}$ and a sweep time of 1 ms. This configuration has been chosen because of the trigger delay of the streak camera: because of this delay, the streak camera cannot be directly trigger by InSb detectors as in the experiments of Pina[5] or Ranc[6], it has to be triggered before the formation of ASB using the signal delivered by the emitter-receiver pairs mounted at the muzzle end of the barrel (Fig.1). Due to the difficulty of precisely evaluate the delay between the the formation of ASB and the trigger signal from emitter-receiver pairs, we chose a long sweep time to not miss the phenomenon. In this configuration, the minimum detectable temperature is 1000 K, in regard of data found in the literature[5,6], we can expect temperatures higher than 1300 K so the streak camera will be able to record the maximum temperature rise.

III. MEASUREMENT UNCERTAINTIES

Although measurement errors induced by the size of the ASB and the variations of surface roughness have been identified by several authors[3,6], we didn't found any precise estimation of the total measurement uncertainty. To evaluate this uncertainty, we first identified the main sources of error and we analysed their combined influences on measurement accuracy.

A. Errors related to spacial resolution

In the present setup, detectors and their optics act as low pass filters of spatial frequencies. In the spatial domain,an image can be calculated as the convolution of the object and the impulse response of the optical system :

$$g_o(x,y) = PSF(x,y) * g_i(x,y) \tag{6}$$

The function $g_i(x,y)$ correspond to the irradiance distribution of an ideal image which is a magnified version of the input-object irradiance, $g_o(x,y)$ is the output-image irradiance distribution, PSF(x,y) is the impulse response of the system also know as the point spread function. Since our detectors perform 1D spatial observations, PSF can be consider along only one direction, in this case we can use the term "line spread function" (LSF). The LSF

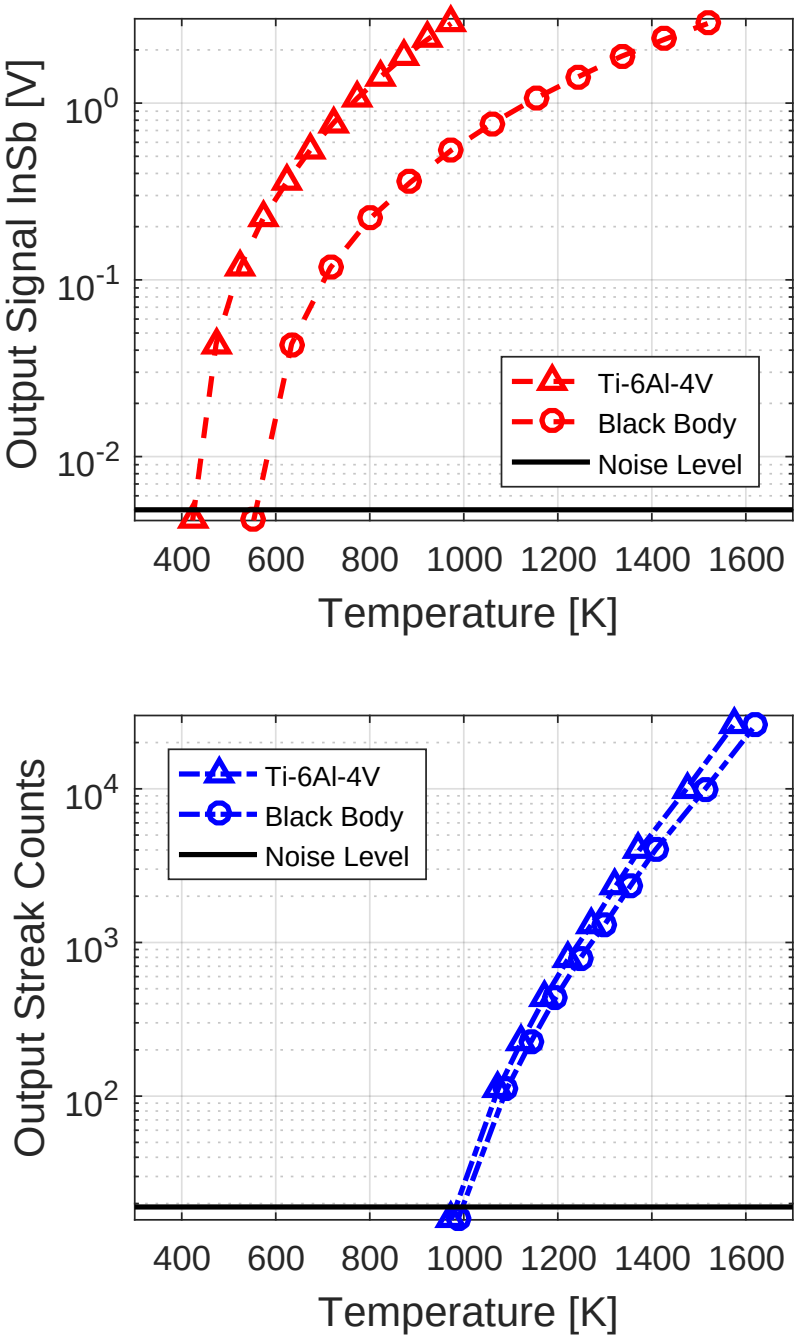

FIG. 4: Calibration curves of Insb detectors and streak camera

will depend on the optical assembly, the finite size of the detectors and the spatial sampling. Instead of using equation (6) it is usually more convenient to work in the spacial frequency domain[14]. By doing so, convolution product turn into a simple product, and equation (6) becomes :

$$\mathscr{F}\left[LSF(x) * g_i(x)\right] = OTF(f_x) \cdot G_i(f_x) \tag{7}$$

where :

$$OTF(f_x) = MTF(f_x) \exp^{iPTF(f_x)} \tag{8}$$

In equation (6), $MTF(f_x)$ is the magnitude response of the imaging system and $PTF(f_x)$ is the phase transfer function. In the following analysis, we will only consider the influence of MTF which can be considere as a product of two functions: the optical modulation transfer function (OMTF) and the detector modulation transfer function (DMTF). The first corresponds to the response of the different optical elements and the second is related to the spatial response of the detector itself.

For the InSb array, DTMF is the product of two functions taking into account the finite dimension of the detectors (Δx_{Det}) and the pitch between two detectors (Δx_{pitch})[15] :

$$DMTF_{InSb}(f_x) = |\operatorname{sinc}(f_x\, \Delta x_{Det})| \cdot |\operatorname{sinc}(f_x\, \Delta x_{pitch})| \tag{9}$$

For the streak camera, the DMTF has a Gaussian profil define as :

$$DMTF_{Streak}(f_x) = \exp\left(-\frac{{f_x}^2}{2{\sigma_x}^2}\right) \tag{10}$$

The parameter σ_{Streak} depends on the performances of the elements constituting the camera (streak tube, micro-channel plate, readout camera) and can be measured experimentally.

For both optical paths, OMTF depends on the diffraction limit and aberrations. These transfer functions are difficult to evaluate analytically, so they have been computed numerically using ray tracing method. In the case of the IR optical path, OMTF essentially depends on the diffraction limit whereas in the VIS-NIR it's the geometric aberrations that limit the resolution. The result of MTF calculations are shown in Figure 5 for an optical magnification of 2 for the IR path and 4 for the VIS-NIR. For IR, the three transfer functions are close to each other and none of them is pre-eminent but for the VIS-NIR, the spacial resolution is essentially limited by the OMTF.

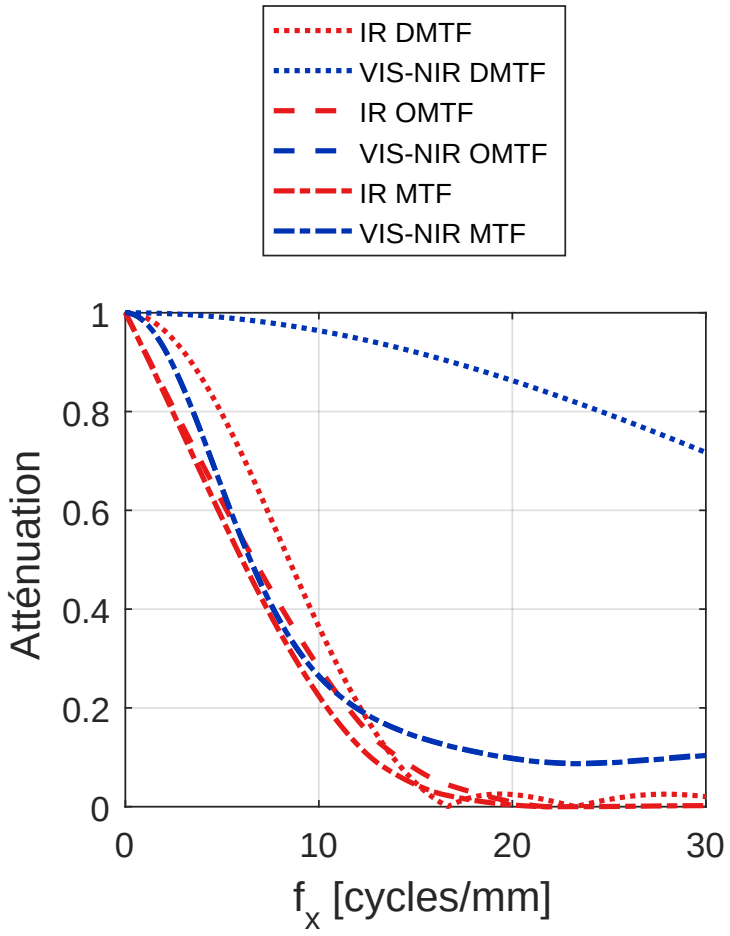

FIG. 5: Optical transfer functions for IR and VIS-NIR (frequencies f_x correspond to the domain of the object plane)

B. Errors related to the temporal response

As for the spacial resolution, the detectors and their electronics act as low pass filters. In regard of the time scale of ASB formation and propagation, inadequate time response can lead to significant errors. The temporal response of each detector can be characterized by its transfer function in the Fourier domain. This function gives informations on the attenuation and phase shift. As for MTF, we will only consider attenuation in our analysis.

In the case of InSb array, detectors and amplifiers behaves like first-order low-pass filters. The temporal modulation transfer function ($H_{InSb}(f)$) can therefore be defined in the

frequency domain as :

$$H_{InSb}(f) = \frac{1}{\sqrt{1+(\frac{f}{f_c})^2}} \tag{11}$$

Where f_c is the cut-off frequency. As explained in section II D, the bandwidth of the InSb amplifier as been reduce to $f_c = 13\,\text{kHz}$ in order to limit the influence of crosstalk effects.

For the streak camera, temporal resolution will depend on the camera architecture but also on the sweep speed and input slit width. The temporal response can be measured by making a static image of the input slit, an example is given in Figure 6. This image shows the dispersion of the photons along the temporal axis which corresponds to a temporal LSF. Because the streak camera performs a temporal to spatial conversion, the sweep speed should be taken into account in order to express the LSF in the temporal domain. The relation between a distance y on the readout camera's focal plane array and the time is :

$$t = v_s \cdot y \tag{12}$$

Where v_s is the sweep speed of the streak unit. In Figure 6, the top horizontal axis correspond to a sweep speed of $50\,\mu\text{s}\,\text{mm}^{-1}$. For our experiments, the temporal LSF can be approximated by a Gaussian distribution :

$$LSF(t) = \frac{1}{(v_s \cdot \sigma_y)\sqrt{2\pi}} \exp\left(\frac{-t^2}{2(v_s \cdot \sigma_y)^2}\right) \tag{13}$$

From this expression, we can express the modulation transfer function ($H_{Streak}(f)$) as:

$$H_{Streak}(f) = \exp\left(\frac{-(f \cdot v_s \cdot \sigma_y)^2}{2}\right) \tag{14}$$

The Fig. 7 shows the transfer function of both detectors. We can see that the streak camera has a much larger bandwidth than InSb detectors. If we consider the response of each detector to a step signal, we find a 10 %-90 % rise time of 27 µs for InSb detectors and 10 µs for the streak camera.

C. Errors related to uncertainties on emissivity

1. Assumptions on emissivity in IR

In IR, uncertainties on emissivity have a strong impact on temperature measurements, so we performed Ti-6Al-4V emissivity measurements in the spectral range $3-5\,\mu\text{m}$ for temperature from $973\,\text{K}$ to $1273\,\text{K}$[12]. We found that emissivity increase slowly and almost linearly

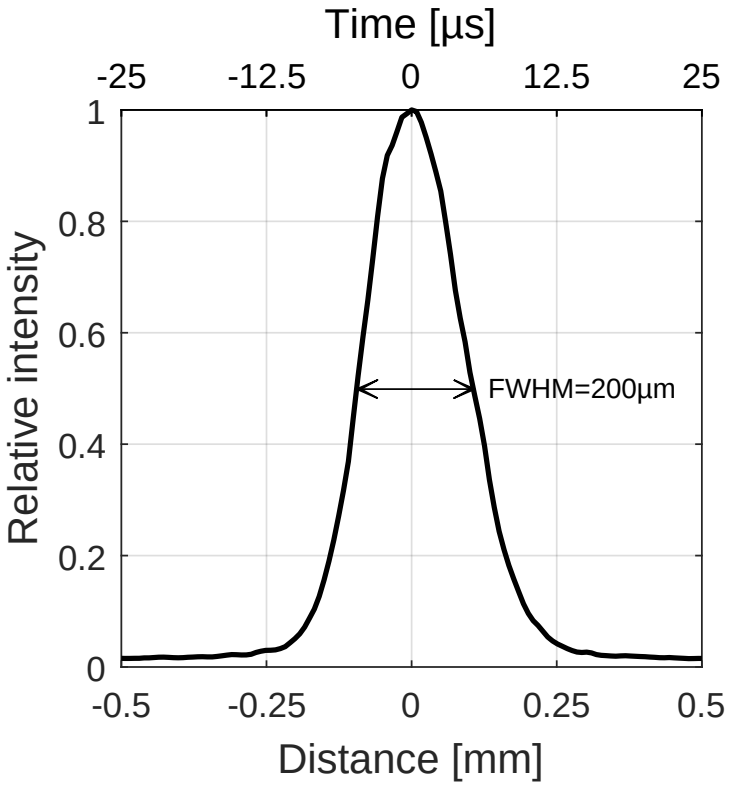

FIG. 6: Static image taken for an input slit width of 25 µm and a sweep speed of $50\,\mu s\,mm^{-1}$

until the transus-β point, at 3 µm, it increase from 0.23 to 0.26 and at 5 µm it is almost constant at 0.2 . These results are consistent with those of González-Fernández and al. which extend to lower temperatures[11], therefore we will consider both set of data to define $\varepsilon(\lambda, T)$.

If it is essential to characterize the emissivity of our material in IR this is not sufficient, because we can suppose that the high strain within ASB will have an influence on $\varepsilon(\lambda, T)$ leading to an error $\frac{\Delta\varepsilon}{\varepsilon}$. This error is difficult to quantify precisely but we can make assumptions on its sign: we can suppose that the high strain within the ASB will always result in an increase of the surface roughness and so, the true value of the emissivity during experiment will be always higher than the one measured statically. The influence of the roughness on the emissivity of Ti-6Al-4V in the spectral range of InSb was studied by Ranc and al.[6] who found a variation of 25 % between a machined and a polished surface. Based on those results, we made the assumption that the true emissivity will always lie in the range of the measured emissivity with an uncertainty of $\varepsilon_{\text{meas}}{}_{0}^{+25\%}$, the resulting uncertainty on

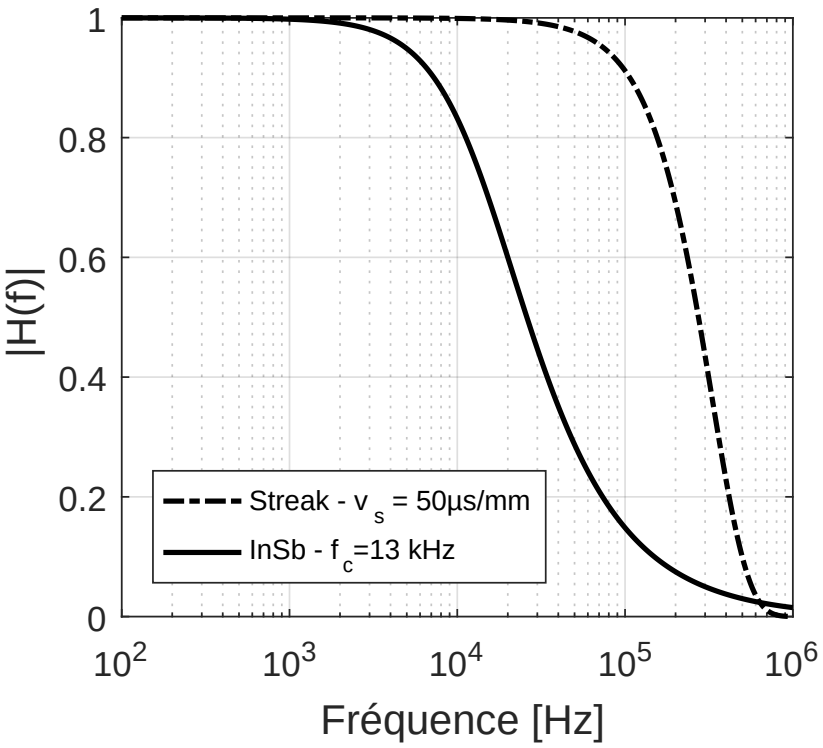

FIG. 7: Temporal transfer function

measured temperature is presented on Fig.8.

2. *Assumptions on emissivity in VIS-NIR*

Because emissivity uncertainty have less impact on temperature measurements in the VIS-NIR range, we based our assumptions on data found in the literature. In the range from 1450 K to 1750 K, Boivineau and al.[16] give a value between 0.56 and 0.6 at a wavelength of 684.5 nm. Milošević and Aleksić[17] give value of-0.53-0.71 in the temperature range from 1300 K to 1750 K at 900 nm. Coppa and Consorti[18] found a value of 0.77 at 1218 K for radiation integrated in the range 0.8 µm-1.1 µm. From these data, we considered that during our experiment the emissivity of Ti-6Al-4V will always lay between 0.5 and 0.75. If we arbitrary choose an emissivity of ε_{meas}=0.625, we can suppose that the true emissivity will always lie in the range $\varepsilon_{\mathrm{meas}}{}^{+20\%}_{-20}$. The resulting range of uncertainties is presented on Fig.8 and we can see that the maximum error is around 2 %.

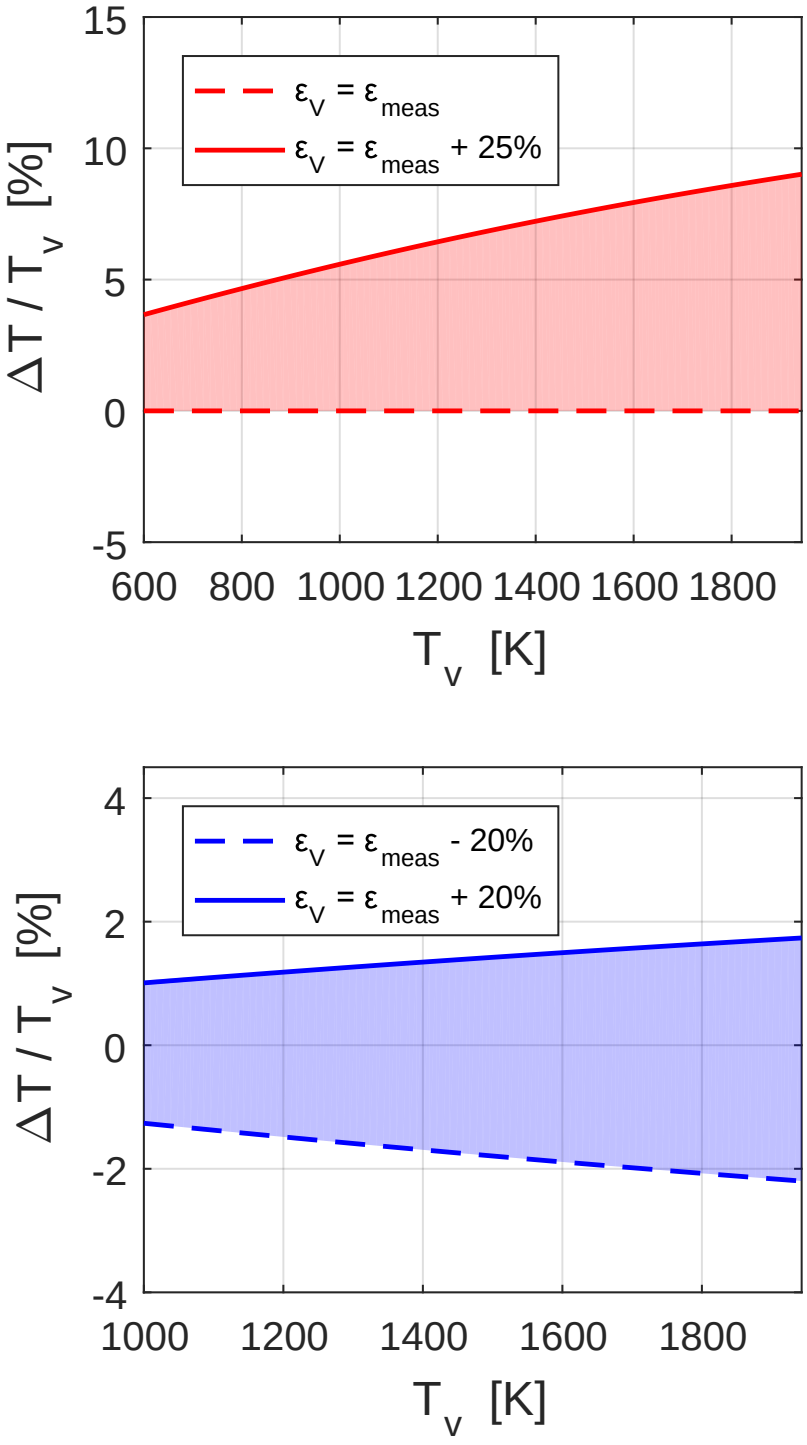

FIG. 8: Uncertainties related to emissivity assumption for InSb (top) and Streak camera (bottom)

D. Total measurement uncertainties of the system

Overestimation of the temperature	Underestimation of the temperature
Emissivity assumptions in IR ($\varepsilon_{meas} < \varepsilon_V$)	Spatial resolution ($f(T_V(x))$)
Emissivity assumptions in VISNIR ($\varepsilon_{meas} < \varepsilon_V$)	Temporal response of detectors ($f(T_V(t))$)
	Emissivity assumptions in VISNIR ($\varepsilon_{meas} > \varepsilon_V$)

TABLE I: Impact of the different error sources on temperature measurements

In previous sections, we identified three main sources of uncertainty. As showed in table I, uncertainties leading to an overestimation of the temperature are only related to emissivity uncertainties and can be easily calculated forom the curves of Fig.8, however in the case of an underestimated temperature, we should take into account the three sources of uncertainties which can be functions of the temperature profile. In regard of the minimum detectable temperatures of the detectors, we know that measurements are made during the third stage of ASB formation. During this stage, ASB are fully formed and we can consider their heat generation profile as Gaussian, we can also suppose that the profile and the volumetric heat generation rate are constant with time[19]. To evaluate the total uncertainty in the case of an underestimated temperature, we simulated the alteration of a theoretical temperature profile as a function of ASB width δ_x (define as the full width at half maximum of the volumetric heat generation profile), rise time t_{pulse} and maximal temperature T_V^{max} (see Fig. 9), the total error is calculated using the theoretical true and measured temperature (see Fig. 9) : we calculated the error on maximum temperature :

$$Error_{tot} = \left| \left(\frac{T_{meas}^{max} - T_V^{max}}{T_V^{max}} \right) \right| \tag{15}$$

Results for each detector is presented on Fig. 10 and 11. These figures show that both detectors uncertainty is more sensitive to δ_x than t_{pulse} and T_V^{max}, we can then conclude that the major source of uncertainties come from the spacial resolution. In order to find the precise value corresponding to our experiments we should take an assumption on δ_x, to do so we performed a series of post-mortem observations[20] on samples impacted at different speeds from $30\,\mathrm{m\,s^{-1}}$ to $60\,\mathrm{m\,s^{-1}}$. Because total uncertainty increase when δ_x decrease, we based our calculations on the minimum measured value which is 121 µm. Considering this, we can estimate a total uncertainty of 15 % for InSb and 7.5 % for the Streak camera.

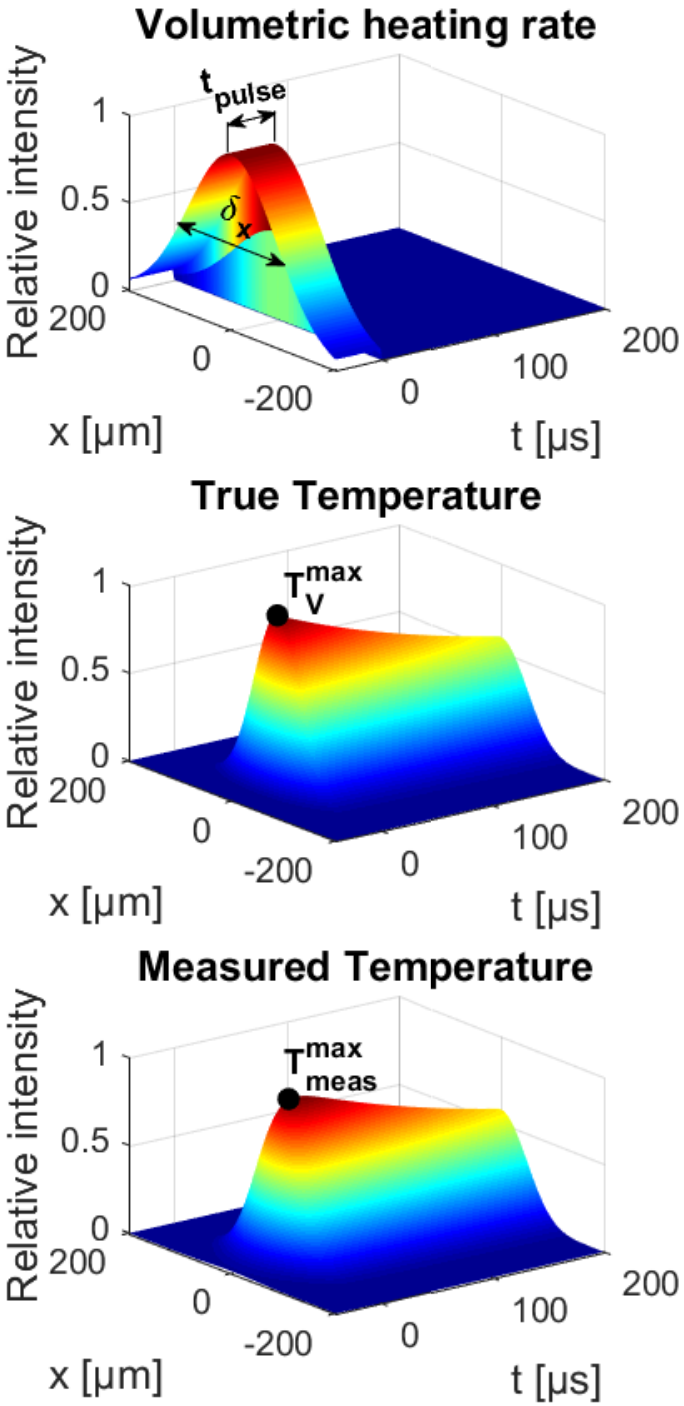

FIG. 9: Parameters of total uncertainties calculation

Preprints (www.preprints.org) | NOT PEER-REVIEWED | Posted: 23 May 2019 doi:10.20944/preprints201905.0286.v1

Peer-reviewed version available at Review of Scientific Instruments 2019, 90; doi:10.1063/1.5112374

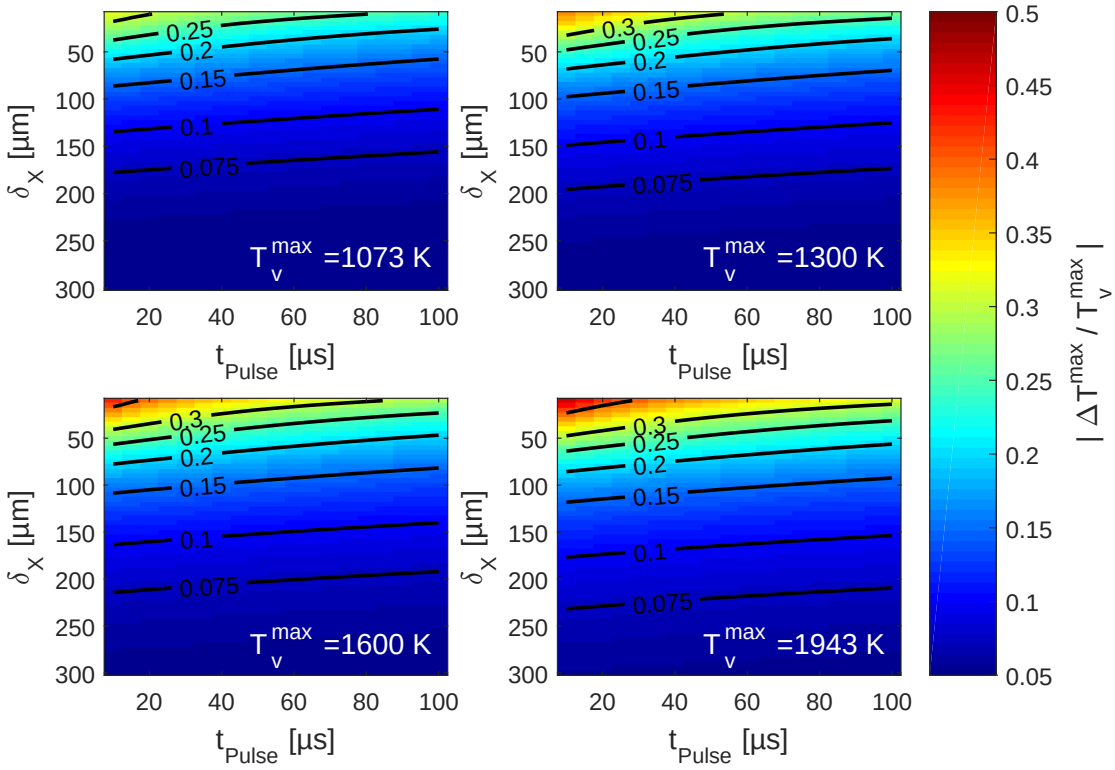

FIG. 10: InSb total uncertainty in the case of an underestimated temperature

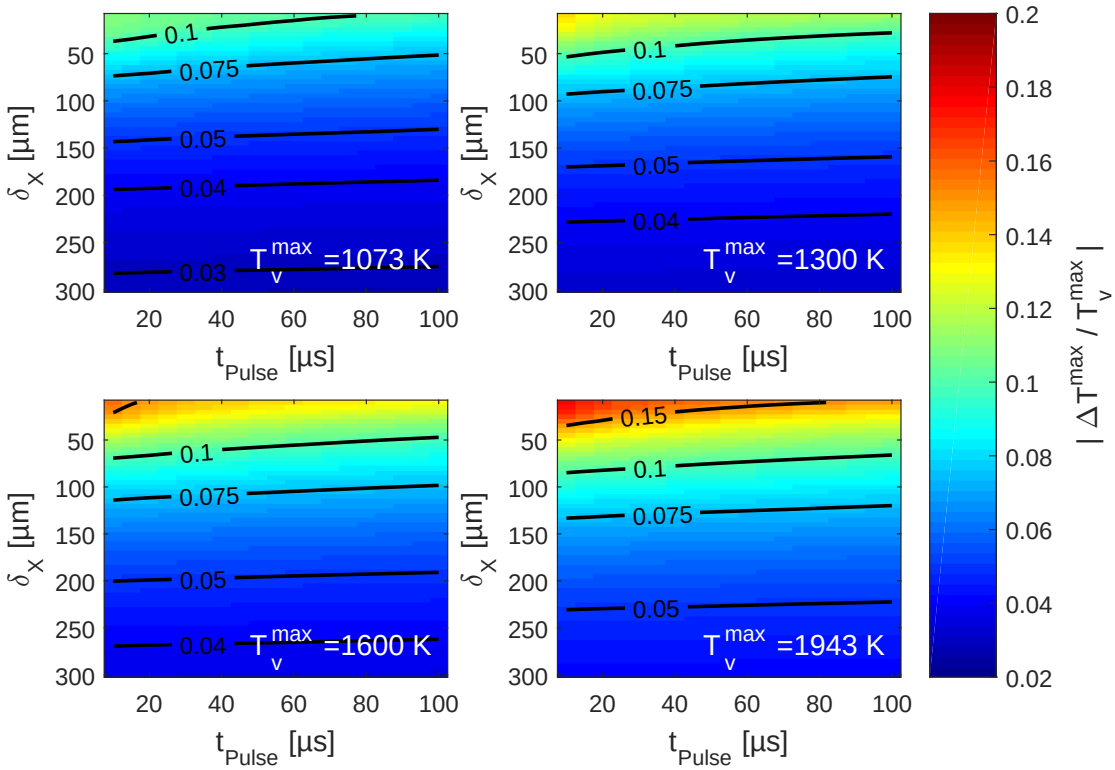

FIG. 11: Streak camera total uncertainty in the case of an underestimated temperature

IV. RESULTS AND DISCUSSIONS

The figure 12 give an example of temperature profiles measured by InSb detectors and streak camera. In order to reduce the noise caused by crosstalk effects, InSb data has been filtered using a low-pass FIR Butterworth filter (cut-off frequency: 57.5 kHz, order: 5) and temperature contour have been interpolated along the spatial axis. The image of the streak camera correspond to a 50 µs/mm sweep speed and was not filtered or interpolated. We arbitrary fixed the origin of spatial and temporal axis at the maximum temperature point. Both profiles present a good similarity and we can identify a hot spot around (−100 µm,−20 µs). As expected, Insb detectors allow measurements on a broader temperature range than streak camera but at the price of higher uncertainty (see Fig. 13). On figure 12, the maximum temperature measured by InSb and streak camera are respectively 1276 K and 1313 K. Those value are coherent with the data of Ranc and al.[6] and Pina[5], however in their work these authors used VIS-NIR intensified camera which was able to take only one 2D image for each test furthermore, the integration time of such camera is problematic for the observation of ASB. The main advantage of the present system is to allow transient observation in both IR and VIS-NIR giving more information on the phenomenon.

In Fig. 13, we present the result of a series of experiment with impactor speed from 28 $\mathrm{m\,s^{-1}}$ to 61 $\mathrm{m\,s^{-1}}$. Error bars have been estimated following the method described in section III. We can clearly see the benefit of short wavelength measurement which present a much smaller range of uncertainties. For all tests, the maximal temperatures measured by InSb detectors tend to be lower than those of the streak camera, this can be imputed to a lower temporal resolution and a lower sensibility of the detectors.

By performing simultaneous measurements in both IR and VIS-NIR spectral range, our system allowed for a precise evaluation of the maximum temperature with a very low influence of emissivity uncertainty. Through a practical case we analyzed the influence of optical assembly and different sources of measurement errors. We detailed the process and steps to present realistic error bars. This approach is relevant to any ASB temperature measurement. Many other applications of this system can be anticipated for the study of ASB or high speed phenomenon (ballistic impact, cold spray, intermetallics reactions).

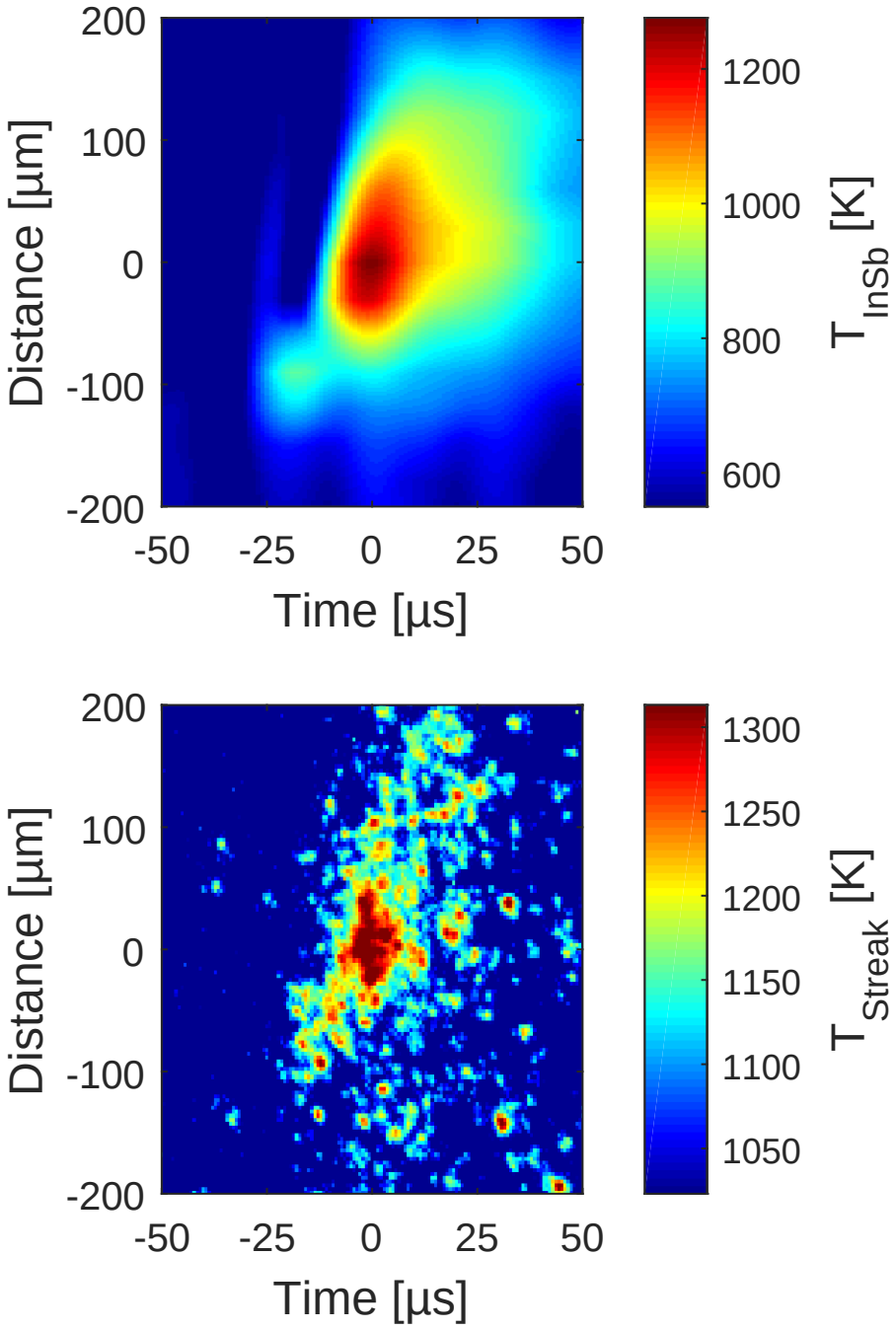

FIG. 12: Measured temperature profiles for an impactor speed of $49\,\mathrm{m\,s^{-1}}$

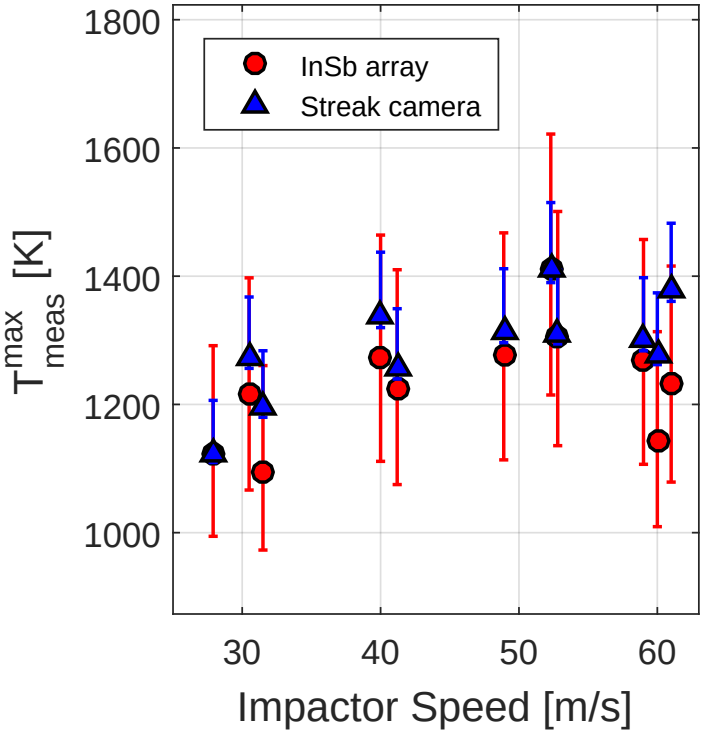

FIG. 13: Maximum measured temperature of each detector for different impactor speed

ACKNOWLEDGEMENT

The authors would like to thank Dr. Nicolas Rambure and Dr. Xingkai Wang for their help in the measurement of Ti-6Al-4V emissivity.

REFERENCES

[1]B. Dodd and Y. Bai, *Adiabatic Shear Localization: Frontiers and Advances* (Elsevier, 2012).

[2]C. Zener and J. H. Hollomon, Journal of Applied Physics **15**, 22 (1944).

[3]A. Marchand and J. Duffy, Journal of the Mechanics and Physics of Solids **36**, 251 (1988).

[4]A. T. Zehnder and A. J. Rosakis, Journal of the Mechanics and Physics of Solids **39**, 385 (1991).

[5]V. Pina, *Mesure de température de bande de cisaillement adiabatique dans des alliages de titane*, Ph.D. thesis, University of Paris X (1997).

[6]N. Ranc, L. Taravella, V. Pina, and P. Hervé, Mechanics of Materials **40**, 255 (2008).

[7]A. T. Zehnder, P. R. Guduru, A. J. Rosakis, and G. Ravichandran, Review of Scientific Instruments **71**, 3762 (2000).

[8]V. Pina, A. Riguet, P. Hervé, and P. Müller, J. Phys. IV France **07**, C3 (1997).

[9]J. E. Miller, T. R. Boehly, A. Melchior, D. D. Meyerhofer, P. M. Celliers, J. H. Eggert, D. G. Hicks, C. M. Sorce, J. A. Oertel, and P. M. Emmel, Review of Scientific Instruments **78**, 034903 (2007).

[10]K. Hartley, J. Duffy, and R. Hawley, Journal of the Mechanics and Physics of Solids **35**, 283 (1987).

[11]L. González-Fernández, E. Risueño, R.B. Pérez-Sáez, and M.J. Tello, Journal of Alloys and Compounds **541**, 144 (2012).

[12]R. Pawelko, J. Cedelle, W. Xingkai, V. Pina, and P. Hervé, in *Société Française de Thermique* (2016).

[13]D. Rittel and Z. Wang, Mechanics of Materials **40**, 629 (2008).

[14]F. Rigollet, R. Reichle, J. Gaspar, J.-L. Gardarein, C. L. Niliot, and R. Huxford, Quantitative InfraRed Thermography Journal **10**, 96 (2013).

[15]G. D. Boreman, *Modulation Transfer Function in Optical and Electro-Optical Systems* (Spie Press Book, 2001).

[16]M. Boivineau, C. Cagran, D. Doytier, V. Eyraud, M. H. Nadal, B. Wilthan, and G. Pottlacher, International Journal of Thermophysics **27**, 507 (2006).

[17]N. Milošević and I. Aleksić, IJMR **103**, 707 (2012).

[18]P. Coppa and A. Consorti, Measurement **38**, 124 (2005).

[19]T. Wright and G. Ravichandran, International Journal of Plasticity **13**, 309 (1997).

[20]R. Pawelko, *Étude des phénomnes thermiques associés à des sollicitations mécaniques à grande vitesse*, Ph.D. thesis, University of Paris X (2018).